Journal of Materials Science & Technology 216 (2025) 93–98

Contents lists available at ScienceDirect

Journal of Materials Science & Technology

journal homepage: www.elsevier.com/locate/jmst

Research Article

Encapsulating Si nanoparticles in ZIF-8-derived carbon through surface amination for stable lithium storage

Le Li[a,b], Jinshuai Liu[a,b], Ruohan Yu[a,b], Ruhan He[a], Jinghui Chen[a,b], Haoqing Ma[a,b], Lei Zhang[a,b], Liqiang Mai[a,b,*], Liang Zhou[a,b,*]

[a] The Sanya Science and Education Innovation Park, Wuhan University of Technology, Sanya 572000, China
[b] State Key Laboratory of Advanced Technology for Materials Synthesis and Processing, Wuhan University of Technology, Wuhan 430070, China

ARTICLE INFO

Article history:
Received 11 May 2024
Revised 17 June 2024
Accepted 25 June 2024
Available online 15 August 2024

Keywords:
Si nanoparticles
Metal-organic frameworks
Surface modification
N-doped carbon
Lithium-ion batteries

ABSTRACT

The application of silicon in lithium-ion batteries has been impaired by the low conductivity and large volume expansion. Herein, we develop a facile "surface amination" strategy to successfully encapsulate Si nanoparticles within the ZIF-8-derived N-doped carbon matrix. The amino group-containing organosilica serves as the linking agent between Si nanoparticles and Zn^{2+} and facilitates the coating of the ZIF-8 layer on the Si nanoparticles. This in turn induces the construction of N-doped carbon matrix encapsulated Si nanoparticles (NH_2-Si@C) during the subsequent carbonization. With buffered volume change and increased conductivity, the rationally designed NH_2-Si@C demonstrates a high reversible capacity (1494 mAh g^{-1} at 1 A g^{-1}) and satisfactory rate performance (1062 mAh g^{-1} at 5 A g^{-1}).

1. Introduction

Nowadays, lithium-ion batteries (LIBs) play an important role in portable electronic devices, electric vehicles, and grid-scale energy storage as the power sources [1–3]. Traditional LIB anode materials based on graphite and $Li_4Ti_5O_{12}$ gradually fail to meet the developing demand due to their low theoretical capacity [4–7]. Consequently, there is a pressing need to develop high-capacity anode materials to meet the growing demands of LIBs.

Silicon has been considered one of the most promising anode materials for LIB in recent years [8–11]. It possesses a high theoretical capacity (4200 mAh g^{-1} for $Li_{22}Si_4$), which is much higher than that of graphite. Moreover, the suitable lithiation potential (0.4 V versus Li/Li^+) and natural abundance of silicon are also the reasons for the high interest from industrial and academic fields [12,13]. However, the alloying reaction of silicon with lithium causes a large volume change. In addition, the low intrinsic conductivity of silicon limits its lithiation/de-lithiation kinetics [14–17]. To address these issues, compositing silicon with carbon has been identified as an effective solution. By incorporating carbon materials, the electrical conductivity can be increased, and the volume expansion of silicon can be buffered [18–20].

Zeolitic imidazolate framework-8 (ZIF-8), a typical metal-organic framework (MOF), is structurally controllable and can be easily synthesized, making it an ideal carbon source [21]. After high-temperature calcination, the ZIF-8 can be converted into an N-doped carbon matrix, which is able to improve the electrical conductivity and limit the volume expansion of silicon. Song et al. [22] designed a ZIF-derived carbon-coated silicon composite anode material. Yang's group [23] employed MOF-derived carbon as the nanoreactor and deposited ultrasmall silicon nanodots within the reactor by chemical vapor deposition (CVD). Zhao's group [24] encapsulated Si nanoparticles in ZIF through a wet-chemistry approach and converted the ZIF/Si composite into Si/C. However, for most reported silicon-carbon composites, the bonding between silicon and carbon is usually relatively weak, which may lead to the detachment of silicon from the carbon matrix during cycling [25,26]. Therefore, it is essential to design a cost-effective and facile method to construct a silicon-carbon structure with high interface stability.

In this study, we develop a surface modification strategy for silicon nanoparticles by introducing amine groups onto the surface (Si-NH_2). Due to the coordination between zinc ions and the amino groups, the Si nanoparticles are successfully encapsulated within ZIF-8 by the self-assembly of zinc ions and 2-methylimidazole (2-MIM). After pyrolysis, the Si nanoparticles are successfully encapsulated in the N-doped carbon matrix derived from the ZIF-8 coating (NH_2-Si@C). The as-prepared NH_2-Si@C delivers a high reversible capacity, stable cycling, and good rate performance.

* Corresponding authors.
E-mail addresses: mlq518@whut.edu.cn (L. Mai), liangzhou@whut.edu.cn (L. Zhou).

https://doi.org/10.1016/j.jmst.2024.06.051
1005-0302/

2. Results and discussion

Fig. 1 illustrates the synthesis process of NH_2-Si@C. The surface amination of Si nanoparticles (denoted as Si NPs) is achieved by dispersing Si NPs (Fig. S1 in Supplementary materials) and (3-aminopropyl)trimethoxysilane (APTMS) in deionized water. The amino groups on the surface of Si NPs can react with Zn^{2+} through a coordination reaction. Meanwhile, the Zn^{2+} assembles with 2-MIM, which leads to the uniform growth of ZIF-8 on the surface of Si NPs. After pyrolysis, the NH_2-Si@C can be obtained. For comparison, a silicon-carbon composite without surface treatment is also prepared (denoted as Si@C).

Fig. 2(a) presents the X-ray diffraction (XRD) patterns of NH_2-Si and pure Si. The characteristic peaks at 28.4°, 47.3°, 56.1°, 69.1°, 76.3°, and 88° can be assigned to the (111), (220), (311), (400), (331), and (422) planes of Si (JCPDS 27–1402) [23]. There is no significant change in the XRD patterns before and after the amination. The Fourier transform infrared (FTIR) spectra of NH_2-Si and Si are shown in Fig. 2(b). Compared to pure Si, the NH_2-Si presents an N–H stretching band at ~ 3500 cm^{-1}, which is from the primary amine group of APTMS [27]. The N 1s X-ray photoelectron spectroscopy (XPS) spectrum of NH_2-Si (Fig. 2(c)) displays an N–H peak (399.2 eV) and a N–C peak (401.3 eV). The Si 2p XPS spectra (Fig. S2) of NH_2-Si show a characteristic peak at 102.5 eV, corresponding to the Si–O–C bond from APTMS. The Si-O-C bond can also be observed in the O 1s XPS spectrum (Fig. S2). The XPS results confirm the coating of APTMS-derived organosilica on the surface of Si. The bare Si NPs are generally spherical in shape and highly aggregated (Fig. 2(d) and S1). After amination, the morphology and size of Si NPs remain (Fig. 2(e)). High-angle annular dark-field scanning transmission electron microscopy (HAADF-STEM) image clearly shows the core@shell structure of NH_2-Si NPs. The corresponding energy dispersive spectrometry (EDS) elemental mappings (Fig. 2(f)) further confirm the core@shell structure and the N mainly distributes on the surface of Si NPs. The formation of the N-rich shell is caused by the hydrolysis and condensation of APTMS on the surface of Si NPs, which forms an organosilica coating. Compared to bare Si NPs (Fig. S1), the NH_2-Si NPs (Fig. 2(f)) show a better dispersion.

The NH_2-Si@ZIF exhibits a well-defined polyhedron shape with a particle size of ~500 nm (Fig. 3(a)). The polyhedron shape of NH_2-Si@ZIF is probably inherited from the usually observed rhombohedral shape of ZIF-8. The polyhedron shape can be generally maintained after carbonization (Fig. 3(b)). Transmission electron microscopy (TEM, Fig. 3(c)) confirms the successful encapsulation of NH_2-Si NPs in the carbon matrix. The (111) lattice fringes of crystalline Si can be clearly observed in the high-resolution TEM (HRTEM, Fig. 3(d)). HAADF-STEM and the corresponding EDS mappings (Fig. 3(e)) further confirm the successful encapsulation of NH_2-Si NPs in the N-doped carbon matrix. Without surface amination, bare Si NPs can also be encapsulated in ZIF-8 (Fig. S3(a)). However, the Si@ZIF core@shell structure collapses after pyrolysis, and a substantial fraction of Si NPs is exposed due to the weak interaction between the Si NPs and ZIF-8 (Figs. S3(b) and S4). That is to say, the coordination between $-NH_2$ and Zn^{2+} plays an important role in maintaining structural stability during carbonization.

Fig. 4(a) presents the XRD patterns of NH_2-Si@ZIF, Si@ZIF, and ZIF-8. All three samples present sharp diffraction peaks between 5°–40°, which belong to ZIF-8 [28]. The two samples after carbonization (NH_2-Si@C and Si@C) show characteristic peaks at 2θ = 28.4°, 47.3°, and 56.1°, which are from crystalline Si (Fig. 4(b)). The absence of any diffractions for graphitic carbon or graphite indicates the amorphous nature of carbon. The Raman spectra of NH_2-Si@C and Si@C display a broad D band (1338 cm^{-1}) and G band (1587 cm^{-1}) with comparable intensities, confirming the amorphous nature of ZIF-8-derived carbon [29]. The Raman spectra of NH_2-Si@C, Si@C, and pure Si (Fig. 4(c)) display sharp bands at 521 cm^{-1}, corresponding to the Si–Si stretching [30]. Thermogravimetric analysis (TGA) is conducted to determine the carbon contents of the samples (Fig. S5). The carbon contents of NH_2-Si@C and Si@C are ~35 and ~38 wt.%, respectively. N_2 sorption is conducted to analyse the specific surface areas and porous structure of NH_2-Si@C and Si@C (Fig. S6). Both NH_2-Si@C and Si@C show type I isotherm, which is typical for microporous materials. The increase in adsorption amount at high P/P_0 is related to the adsorption of N_2 at the interparticle voids. Hysteresis loops can also be observed at relatively high P/P_0 values. The Brunauer-Emmett-Teller (BET) surface areas of NH_2-Si@C and Si@C are calculated to be 399 and 410 $m^2\ g^{-1}$.

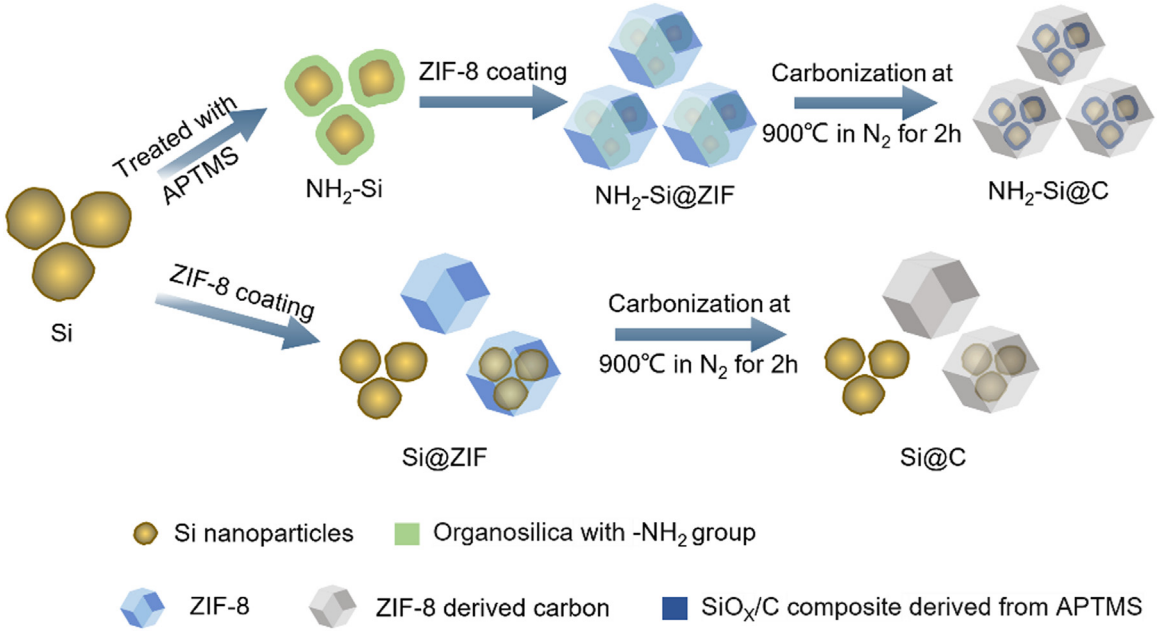

Fig. 1. Schematic illustration for the synthesis of NH_2-Si@C and Si@C.

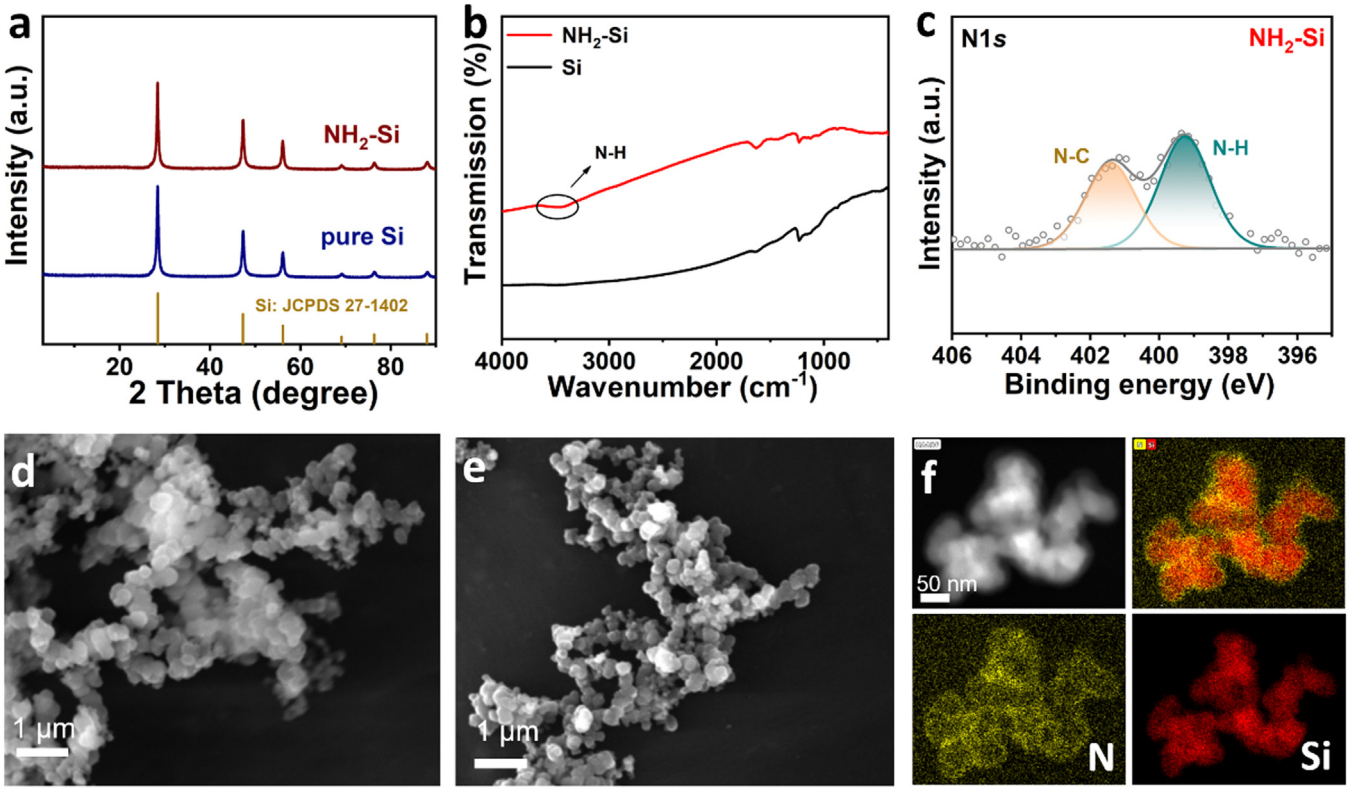

Fig. 2. (a) XRD patterns of NH_2-Si and pure Si, (b) FTIR spectra of NH_2-Si and Si; (c) N 1s XPS spectrum of NH_2-Si; (d) SEM image of Si NPs; (e) SEM image of NH_2-Si; (f) HAADF-STEM image and the corresponding EDS mappings of NH_2-Si.

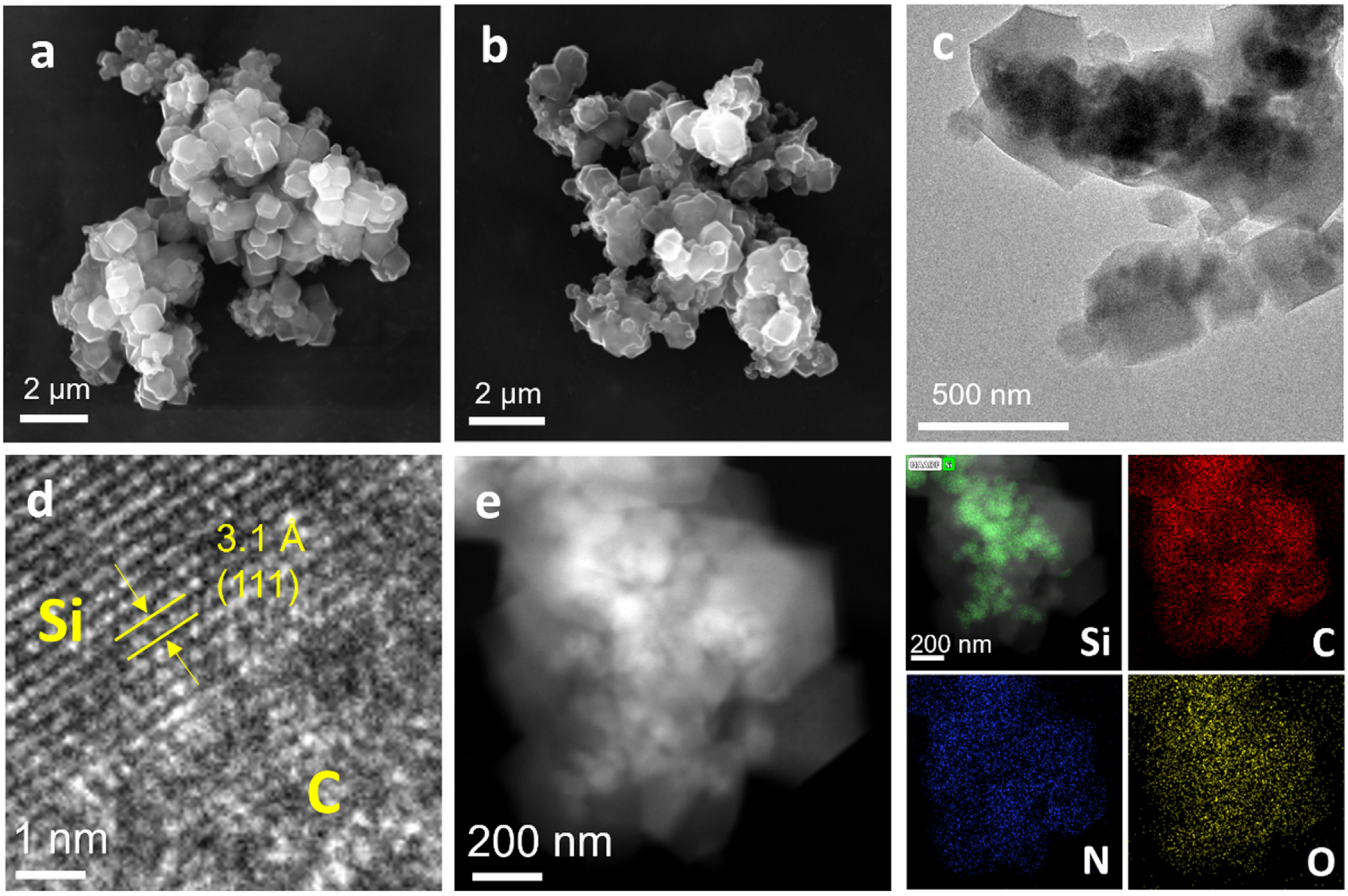

Fig. 3. (a) SEM image of NH_2-Si@ZIF, (b) SEM, (c) TEM, (d) HRTEM, and (e) HAADF-STEM image and the corresponding EDS mappings of NH_2-Si@C.

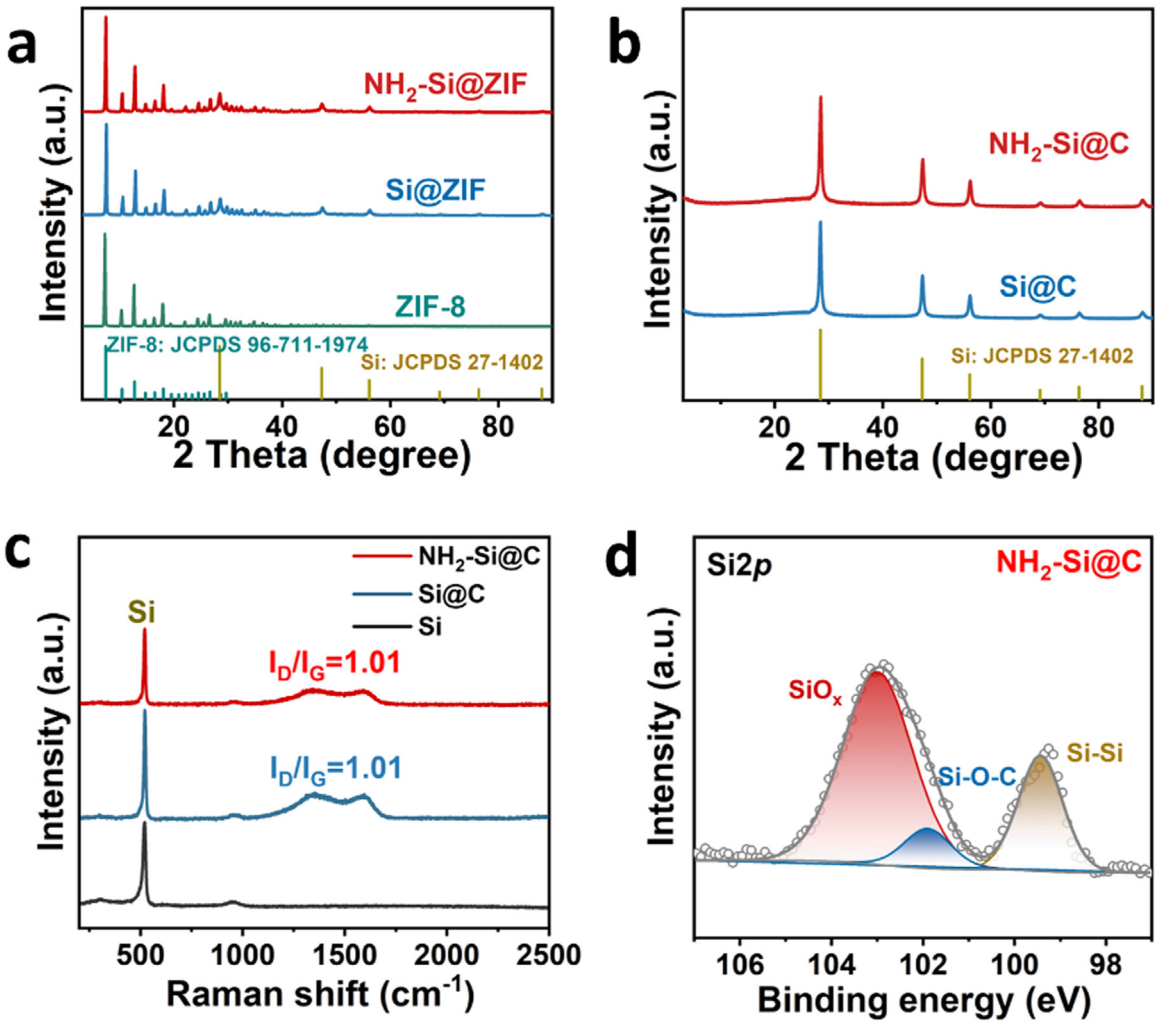

Fig. 4. (a) XRD patterns of NH_2-Si@ZIF, Si@ZIF, and ZIF-8; (b) XRD patterns of NH_2-Si@C and Si@C; (c) Raman spectra of NH_2-Si@C, Si@C, and Si; (d) Si 2p XPS spectrum of NH_2-Si@C.

The XPS survey spectrum of NH_2-Si@C (Fig. S7(a)) shows peaks for C, N, O, and Si elements. The Si 2p spectrum (Fig. 4(d)) of NH_2-Si@C shows three distinct components at 99.4, 101.9, and 102.9 eV, which are from the Si–Si, Si–O–C, and SiO_x species, respectively [31]. The N 1s spectrum (Fig. S7(b)) presents three distinct nitrogen species, corresponding to N–H, N–C, and N=C species with characteristic binding energies of 398.7, 400.9, and 403.5 eV, respectively. The C 1s spectrum (Fig. S7(c)) exhibits three carbon species, attributed to C–C (284.8 eV), C–N/C–O (286.3 eV), and C=O (288.8 eV). Moreover, the O 1s spectrum (Fig. S7(d)) showcases three oxygen species, identified as C=O, Si–O–C, and Si–O–Si with binding energies of 530.6, 531.9, and 533.2 eV, respectively.

The cyclic voltammetry (CV, Fig. 5(a)) curves of NH_2-Si@C exhibit a reduction peak at 0.4 V in the first discharge process, arising from the decomposition of fluoroethylene carbonate (FEC) and the generation of a solid electrolyte interphase (SEI) film. The disappearance of this peak in the subsequent cycles indicates the ideal stability of the SEI film [32,33]. In addition, a cathodic peak at 0.01 V corresponding to the alloying reaction of Si can also be observed. The oxidation peaks at 0.33 and 0.51 V in the first anodic process resulted from the de-alloying reaction from Li_xSi to amorphous Si [34]. As the crystalline Si is transformed into amorphous Si during the first cycle, a reduction peak from the alloying process of amorphous Si is observed at 0.19 V in the subsequent cycles. Fig. S8(a) provides the CV profiles of Si@C for comparison. The Si@C shows CV profiles quite similar to those of NH_2-Si@C.

Representative galvanostatic charge/discharge (GCD) profiles of NH_2-Si@C are displayed in Fig. 5(b). At 0.2 A g^{-1}, the NH_2-Si@C manifests a high initial discharge capacity of 2408 mAh g^{-1} and an initial Coulombic efficiency of 75.8 %. At the same current density, the Si@C exhibits a slightly lower capacity (2261 mAh g^{-1}) as well as ICE (75.2 %) (Fig. S8(b)). Fig. 5(c) compares the cycling performances of NH_2-Si@C and Si@C at 0.2 A g^{-1}. The NH_2-Si@C demonstrates not only a higher capacity but also better cyclability than the Si@C. From the 2nd cycle to the 100th cycle, the capacity fading for NH_2-Si@C and Si@C are 24.6 % and 41.1 %, respectively. The better cyclability of NH_2-Si@C can be attributed to its full encapsulation structure, which effectively restricts the volume expansion of Si NPs. Over 300 cycles at 1 A g^{-1}, the NH_2-Si@C retains 66.3 % of the reversible capacity, while the Si@C retains only 40.4 % (Fig. 5(d)). For the rate performance (Fig. 5(e)), the NH_2-Si@C delivers capacities of 1768, 1702, 1573, 1459, 1369, and 1062 mAh g^{-1} at 0.1, 0.2, 0.5, 1, 2, and 5 A g^{-1}, respectively. The capacity recovers to 1676 mAh g^{-1} with the switching back of current density to 0.2 A g^{-1}. Although the capacity of Si@C is just slightly lower than that of NH_2-Si@C at low current densities, the capacity difference exacerbates with increasing current density. In short, the NH_2-Si@C outperforms the Si@C in capacity, cyclability, and rate capability. In addition, compared to other Si/ZIF-derived anode materials, the

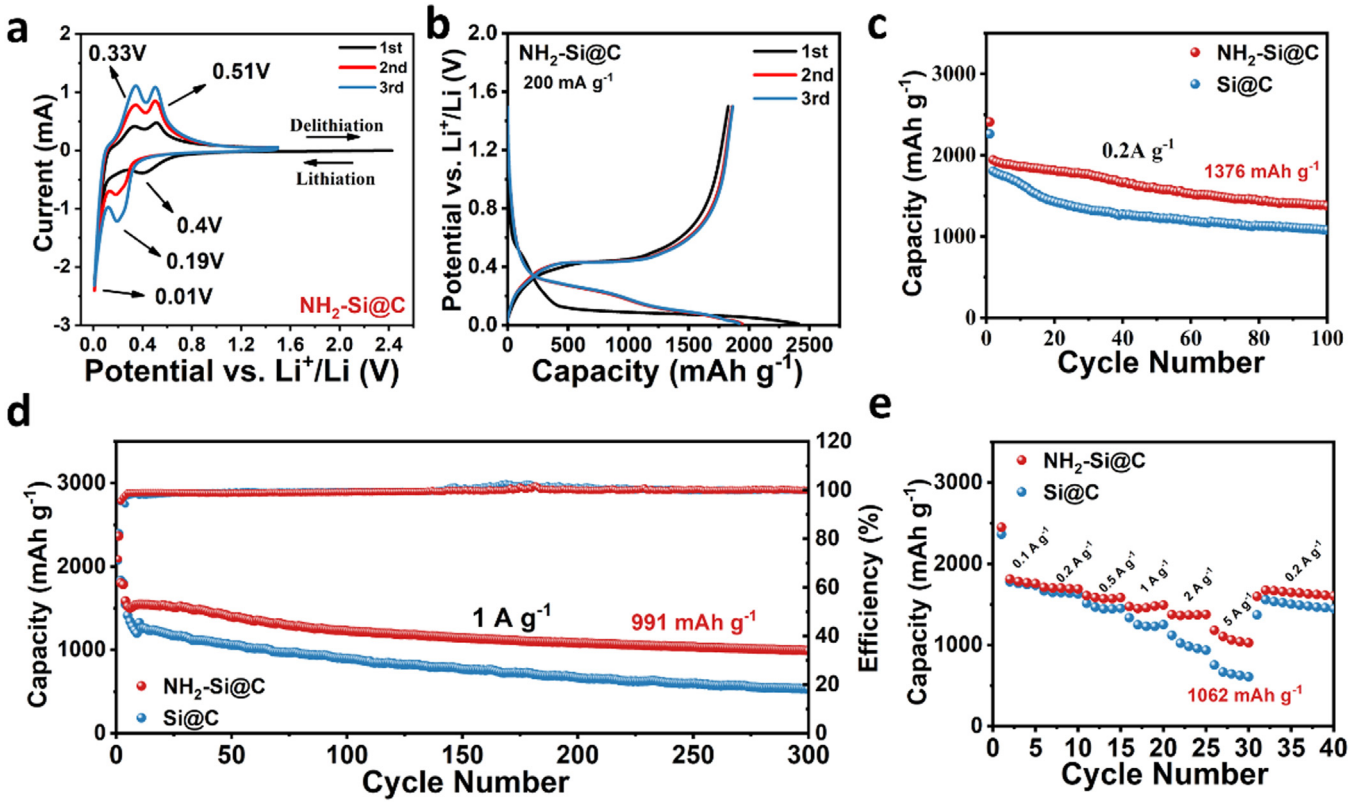

Fig. 5. (a) CV profiles and (b) representative GCD profiles of NH_2-Si@C. Cycling performances of NH_2-Si@C and Si@C at (c) 200 mA g^{-1} and at (d) 1 A g^{-1}. (e) Rate performances of NH_2-Si@C and Si@C. For (d), the samples are activated at 200 mA g^{-1} for 5 cycles and then cycled at 1 A g^{-1}.

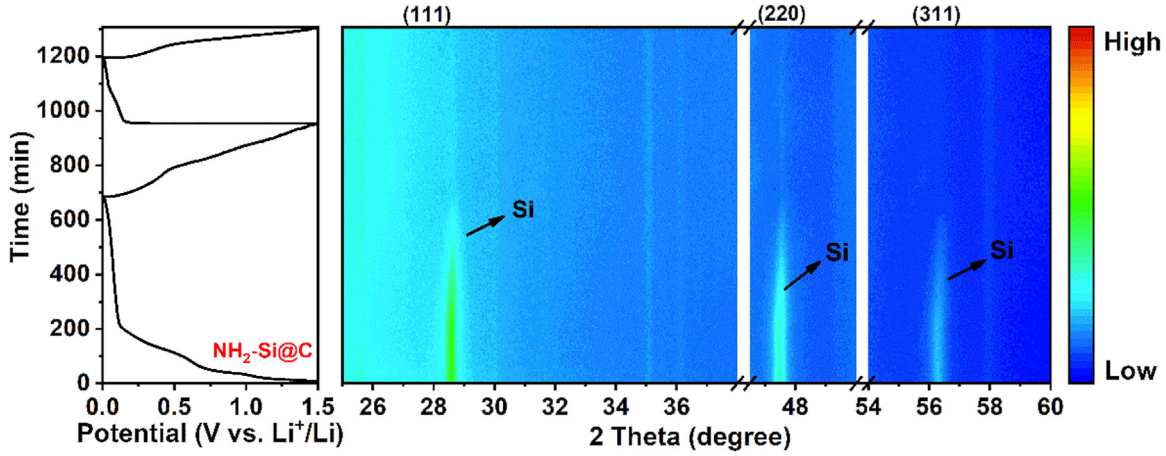

Fig. 6. *In-situ* XRD patterns of the NH_2-Si@C collected during GCD at 300 mA g^{-1}.

NH_2-Si@C also demonstrates comparable, if not superior, electrochemical performances (Table S1).

To find out the optimized Si to ZIF ratio, the ZIF feeding amount (2-MIM and zinc nitrate) is tuned from 0.005 to 0.02 mol, while the NH_2-Si feeding amount is fixed at 200 mg. The optimal electrochemical performance of NH_2-Si@C is achieved with a ZIF content of 0.01 mol, striking a balance between capacity and stability (Fig. S9).

Electrochemical impedance spectra (EIS, Fig. S10) demonstrate that the NH_2-Si@C has a lower charge transfer resistance (R_{ct}) than the Si@C [35]. The structural stability of the electrodes is investigated through ex-situ SEM (Figs. S11 and S12). Severe cracking of the Si@C-based electrode can be observed after 50 cycles (Fig. S11(d)). Meanwhile, the electrode thickness increases dramatically from 14.3 to 19.9 μm with a thickness expansion of 39.2 % (Fig. S12(d)). In contrast, the NH_2-Si@C-based electrode exhibits excellent structural integrity (Fig. S11(b)). The thickness of the electrode increases slightly from 8.1 to 9.4 μm after 50 cycles, showing an alleviated thickness expansion of 14.3 % (Fig. S12(b)). *Ex-situ* TEM reveals that the NH_2-Si@C (Fig. S13) retains its well-defined core@shell structure after 100 cycles at 1 A g^{-1}. In contrast, the Si@C undergoes severe structural degradation, as evidenced by the pulverization of the material into a fractured morphology (Fig. S14).

The Li^+ diffusivity in the NH_2-Si@C and Si@C is investigated by galvanostatic intermittent titration technique (GITT, Fig. S15). Based

on the Fick's second law, the diffusion coefficient of Li^+ (D_{Li^+}) is calculated according to the following simplified equation:

$$D_{Li^+} = \frac{4L^2}{\pi\tau}\left(\frac{\Delta E_S}{\Delta E_\tau}\right)^2 \quad (1)$$

where L refers to the Li^+ diffusion length (equal to the electrode thickness), ΔE_τ represents the voltage change, and ΔE_S is the voltage change induced by the pulse [36]. Fig. S14(b) displays the D_{Li^+} values of NH_2-Si@C and Si@C at different times. The NH_2-Si@C shows a slightly higher D_{Li^+} value than the Si@C. Throughout the dealloying process, the D_{Li^+} of the NH_2-Si@C electrode is relatively constant with a value as high as $\sim 10^{-11}$ cm^2 s^{-1}, higher than that of the Si@C electrode (10^{-12} cm^2 s^{-1}).

In-situ XRD is performed to elucidate the structural evolution of NH_2-Si@C during the GCD process (Fig. 6). The electrode at open circuit voltage (OCV) exhibits distinct characteristic peaks from Si (28.4°, 47.3°, and 56.1°). During the initial discharge, the intensity of the diffraction peaks from Si decreases continuously, which is caused by the alloying reaction of Si [37]. Upon completion of the initial discharge process, the crystalline Si undergoes a phase transformation, converting into amorphous Li_xSi, as evidenced by the disappearance of characteristic diffraction peaks in the XRD patterns (Fig. S16). Notably, the amorphous nature of Li_xSi persists throughout the subsequent charge-discharge cycles [38].

3. Conclusions

In summary, Si nanoparticles encapsulated in a ZIF-8-derived N-doped carbon matrix (NH_2-Si@C) have been successfully constructed by a facile surface amination approach. The obtained material manifests high reversible capacity (1494 mAh g^{-1}, at 1 A g^{-1}), decent rate performance (1062 mAh g^{-1}, at 5 A g^{-1}), and good cycling performance (991 mAh g^{-1} after 300 cycles at 1 A g^{-1}). This work develops a strategy to encapsulate Si nanoparticles in carbon, which could alleviate the inherent volume expansion and low conductivity issues of Si.

Declaration of competing interest

The authors declare that they have no known competing financial interests or personal relationships that could have appeared to influence the work reported in this paper.

CRediT authorship contribution statement

Le Li: Writing – original draft, Visualization, Validation, Supervision, Software, Resources, Project administration, Methodology, Investigation, Funding acquisition, Formal analysis, Data curation, Conceptualization. **Jinshuai Liu:** Writing – review & editing, Supervision, Formal analysis. **Ruohan Yu:** Writing – review & editing, Supervision, Formal analysis. **Ruhan He:** Writing – review & editing, Supervision, Formal analysis. **Jinghui Chen:** Writing – review & editing, Supervision, Formal analysis. **Haoqing Ma:** Formal analysis, Data curation. **Lei Zhang:** Supervision, Funding acquisition. **Liqiang Mai:** Supervision, Funding acquisition. **Liang Zhou:** Writing – review & editing, Supervision, Funding acquisition.

Acknowledgements

This work was financially supported by the Hainan Provincial Joint Project of Sanya Yazhou Bay Science and Technology City (No. 2021JJLH0069), the Project of Sanya Yazhou Bay Science and Technology City (grant No SCKJ-JYRC-2023–55), and the Hainan Provincial Natural Science Foundation of China (No. 522CXTD516).

Supplementary materials

Supplementary material associated with this article can be found, in the online version, at doi:10.1016/j.jmst.2024.06.051.

References

[1] M. Li, J. Lu, Z. Chen, K. Amine, Adv. Mater. 30 (2018) 1800561.
[2] G. Zubi, R. Dufo-López, M. Carvalho, G. Pasaoglu, Renew. Sust. Energ. Rev. 89 (2018) 292–308.
[3] J. Xie, Y.C. Lu, Nat. Commun. 11 (2020) 2499.
[4] S. Chae, S.H. Choi, N. Kim, J. Sung, J. Cho, Angew. Chem. Int. Ed. 59 (2020) 110–135.
[5] P. Li, H. Kim, S.T. Myung, Y.K. Sun, Energy Stor. Mater. 35 (2021) 550–576.
[6] Y. Liu, H. Shi, Z.S. Wu, Energ. Environ. Sci. 16 (2023) 4834–4871.
[7] J. Zhuang, X. Xu, G. Peleckis, W. Hao, S.X. Dou, Y. Du, Adv. Mater. 29 (2017) 1606716.
[8] J. Guo, D. Dong, J. Wang, D. Liu, X. Yu, Y. Zheng, Z. Wen, W. Lei, Y. Deng, J. Wang, G. Hong, H. Shao, Adv. Funct. Mater. 31 (2021) 2102546.
[9] Z. Cheng, H. Jiang, X. Zhang, F. Cheng, M. Wu, H. Zhang, Adv. Funct. Mater. 33 (2023) 2301109.
[10] J.I. Lee, Y. Ko, M. Shin, H.K. Song, N.S. Choi, M.G. Kim, S. Park, Energ. Environ. Sci. 8 (2015) 2075–2084.
[11] N. Liu, Z. Lu, J. Zhao, M.T. McDowell, H.W. Lee, W. Zhao, Y. Cui, Nat. Nanotechnol. 9 (2014) 187–192.
[12] Z. Liu, Q. Yu, Y. Zhao, R. He, M. Xu, S. Feng, S. Li, L. Zhou, L. Mai, Chem. Soc. Rev. 48 (2019) 285–309.
[13] W. An, B. Gao, S. Mei, B. Xiang, J. Fu, L. Wang, Q. Zhang, P.K. Chu, K. Huo, Nat. Commun. 10 (2019) 1447.
[14] H.J. Lee, J.S. Moon, Y.W. Byeon, W.Y. Yoon, H.K. Kim, J.P. Ahn, ACS Energy Lett 7 (2022) 2469–2476.
[15] Q. Wang, M. Zhu, G. Chen, N. Dudko, Y. Li, H. Liu, L. Shi, G. Wu, D. Zhang, Adv. Mater. 34 (2022) 2109658.
[16] Q. Wang, T. Meng, Y. Li, J. Yang, B. Huang, S. Ou, C. Meng, S. Zhang, Y. Tong, Energy Stor. Mater. 39 (2021) 354–364.
[17] R. Yu, Y. Pan, Y. Liu, L. Zhou, D. Zhao, J. Wu, L. Mai, ACS Nano 17 (2023) 2568–2579.
[18] R. Yu, Y. Pan, Y. Jiang, L. Zhou, D. Zhao, G. Van Tendeloo, J. Wu, L. Mai, Adv. Mater. 35 (2023) 2306504.
[19] R. Gao, J. Tang, X. Yu, S. Tang, K. Ozawa, T. Sasaki, L.C. Qin, Nano Energy 70 (2020) 104444.
[20] R. He, H. Li, A. Chen, L. Mai, L. Zhou, J. Mater. Sci. Technol. 191 (2024) 17–22.
[21] Y. Pan, Y. Liu, G. Zeng, L. Zhao, Z. Lai, ChemComm. 47 (2011) 2071–2073.
[22] Y. Song, L. Zuo, S. Chen, J. Wu, H. Hou, L. Wang, Electrochim. Acta 173 (2015) 588–594.
[23] B. Chen, L. Chen, L. Zu, Y. Feng, Q. Su, C. Zhang, J. Yang, Adv. Mater. 34 (2022) 2200894.
[24] L. Zhang, Q. Huang, X. Liao, Y. Dou, P. Liu, M. Al-Mamun, Y. Wang, S. Zhang, S. Zhao, D. Wang, G. Meng, H. Zhao, Energ. Environ. Sci. 14 (2021) 3502–3509.
[25] Q. Li, Y. Wang, X. Gao, H. Li, Q. Tan, Z. Zhong, F. Su, J. Alloys Compd. 872 (2021) 159712.
[26] X. Niu, C. Wang, W. Zhang, D. Wang, H. Shi, L. Yu, C. Wang, Z. Xiong, Z. Ji, Y. Gao, X. Yan, Electrochim. Acta 403 (2022) 139671.
[27] G. Huang, D.M. Yin, L.M. Wang, J. Mater. Chem. A 4 (2016) 15106–15116.
[28] H. Liu, Y. Zhang, J. Dong, T. Ye, J. Hao, Y. Yang, X. Jiang, X. Kang, Y. Bando, X. Wang, J. Mater. Chem. A 6 (2018) 14894–14902.
[29] J.Z. Chen, S.G. Wang, Y.L. Hou, W.X. Wen, H.Y. Wang, B.H. Zhang, D.L. Zhao, J. Energy Storage 74 (2023) 109356.
[30] G. Hu, R. Yu, Z. Liu, Q. Yu, Y. Zhang, Q. Chen, J. Wu, L. Zhou, L. Mai, ACS Appl. Mater. Interfaces 13 (2021) 3991–3998.
[31] Y. Ren, M. Li, J. Power Sources 306 (2016) 459–466.
[32] C. Zhu, Y. Zhang, Z. Wu, Z. Ma, X. Guo, F. Guo, J. Zhang, Y. Li, J. Mater. Sci. Technol. 87 (2021) 18–28.
[33] Q. Wei, Y.M. Chen, X.J. Hong, C.L. Song, Y. Yang, L.P. Si, M. Zhang, Y.P. Cai, Appl. Surf. Sci. 511 (2020) 145609.
[34] X. Fan, T. Cai, S. Wang, Z. Yang, W. Zhang, Small 19 (2023) 2300431.
[35] Y.S. Kim, Y.L. Joo, Y.J. Kwark, J. Mater. Sci. Technol. 32 (2016) 195–199.
[36] Q. Ouyang, G. Li, X. Zhang, X. Zhao, Y. Wang, Q. Wang, Z. Fan, J. Wang, L. Li, Chem. Eng. J. 460 (2023) 141762.
[37] H. Du, R. Yu, X. Tan, J. Wu, D. Zhao, L. Mai, L. Zhou, Sci. China Mater. 66 (2023) 2199–2206.
[38] Z. Jia, T. Li, J. Mech. Phys. Solids 91 (2016) 278–290.